Journal of Power Sources 654 (2025) 237832

Contents lists available at ScienceDirect

Journal of Power Sources

journal homepage: www.elsevier.com/locate/jpowsour

Synergistic thermal expansion reduction in cobalt-containing perovskite cathodes for solid oxide fuel cells

Nilam Shah [a], Tianjiu Zhu [a], Xiaoyong Xu [b,*], Hao Wang [c], Zhonghua Zhu [a,**], Lei Ge [c,d,***]

[a] School of Chemical Engineering, The University of Queensland, Brisbane, 4072, QLD, Australia
[b] School of Chemical Engineering, University of Adelaide, Adelaide, 5000, SA, Australia
[c] Centre for Future Materials, University of Southern Queensland, Springfield, QLD, 4300, Australia
[d] School of Engineering, University of Southern Queensland, Springfield, QLD, 4300, Australia

HIGHLIGHTS

- Synergistic strategy to reduce thermal expansion and enhance stability.
- Improved compatibility through thermal expansion offset.
- Enhanced thermal cycling resistance and structural integrity.
- Suppression of cobalt reduction mitigated chemical expansion.
- Potential strategy for improving durability across SOFC cathode materials.

GRAPHICAL ABSTRACT

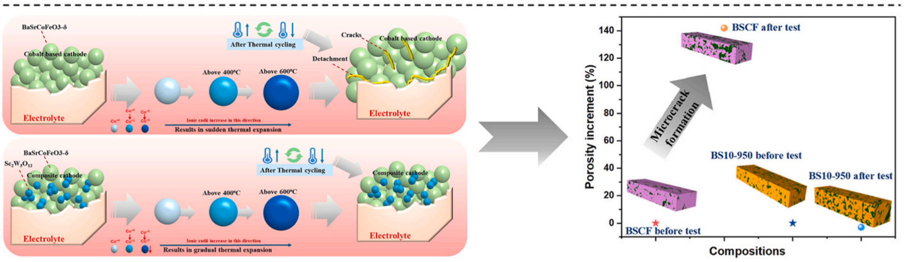

ABSTRACT

$SrCoO_{3-\delta}$ -based cathodes, such as $Ba_{0.5}Sr_{0.5}Co_{0.8}Fe_{0.2}O_{3-\delta}$ (BSCF), exhibit high oxygen reduction reaction (ORR) activity, making them strong candidates for solid oxide fuel cells (SOFCs). However, their high thermal expansion leads to significant mechanical degradation during thermal cycling, hindering their broader application. In this study, we introduced a synergistic strategy by incorporating negative thermal expansion material $Sc_2W_3O_{12}$ (ScWO) into BSCF to reduce the overall thermal expansion of composite cathode. The thermal expansion offset strategy together with the suppression of cobalt reduction at the elevated temperature, contributes for maintaining thermal compatibility in cobalt-based cathode and the cathode/electrolyte interface. Over 40 thermal cycles between 600 and 300°C, BSCF showed more than 100 % ASR degradation, while the composite cathode demonstrated just 18 % degradation, indicating enhanced thermal cycling resistance. Microstructural analysis using FIB-SEM revealed approximately 140 % relative porosity increase in BSCF due to microcracking. In contrast, negligible porosity change was observed in the composite cathode, confirming the benefit to the overall structural integrity.

1. Introduction

Solid Oxide Fuel Cells (SOFCs) are one of the promising modern energy conversion and clean power generation technologies, attracting attention for their fuel flexibility, high efficiency, and the absence of expensive noble metal catalysts [1,2]. Their adaptability positions SOFCs as viable solutions for diverse applications, spanning stationary power generation to portable devices. However, the commercial

---

* Corresponding author.
** Corresponding author.
*** Corresponding author. Centre for Future Materials, University of Southern Queensland, Springfield, QLD, 4300, Australia.

E-mail addresses: xiaoyong.xu@adelaide.edu.au (X. Xu), z.zhu@uq.edu.au (Z. Zhu), lei.ge@usq.edu.au (L. Ge).

https://doi.org/10.1016/j.jpowsour.2025.237832
Received 19 February 2025; Received in revised form 2 June 2025; Accepted 3 July 2025

viability of SOFCs is often challenged by the integrity of the cell structure and the electrochemical stability of the cathode [3–6]. Cobalt-containing perovskite cathodes, such as Barium Strontium Cobalt Ferrite (BSCF), are renowned due to their ability to leverage multiple cobalt oxidation states for rapid redox cycling, coupled with mixed ionic-electronic conductivity (MIEC) that enhances oxygen ion mobility and overall catalytic activity [7–9]. Furthermore, the perovskite structure allows for extensive doping, facilitating the optimization of both stability and oxygen reduction reaction (ORR) activity [10,11].

Despite these advantages, the practical use of cobalt-based perovskites in SOFCs is limited by their high thermal expansion coefficient (TEC) [12–16], which can cause mechanical and structural issues during operation [17]. For instance, BSCF exhibits a TEC in the range of 20–25 $\times 10^{-6}$ K^{-1}, significantly higher than typical SOFC electrolytes like yttria-stabilized zirconia (YSZ) and samarium-doped ceria (SDC), which have TECs around 10-11 $\times 10^{-6}$ K^{-1}. Reducing cobalt ions from higher oxidation states to Co^{2+} during high-temperature operation leads to lattice expansion and increased TEC [18–20], which generates significant mechanical stress. This increased stress is due to the TEC disparity between the cathode and other SOFC components, potentially leading to thermo-mechanical degradation and delamination at electrode\electrolyte interfaces [21–23]. The high TEC and mechanical instability, particularly during frequent start-up and shutdown cycles, reduce the SOFC's operational lifetime and reliability [24,25].

To mitigate these challenges, strategies such as doping, cation deficiency creation, and the incorporation of negative thermal expansion (NTE) materials and/or electrolyte materials have been explored. Doping elements into the perovskite structure can reduce TEC while maintaining ORR catalytic activity, though complete replacement of cobalt often compromises performance [26]. Additionally, incorporating low thermal expansion electrolyte materials can expand the triple-phase boundary, which is crucial for ORR. However, this approach alone often does not meet expectations in sufficiently reducing the TEC [27,28]. Therefore, designing composite cathodes containing negative NTE materials is a promising strategy to address the high TECs, an intrinsic characteristic of cobalt-containing perovskites. By integrating NTE materials such as $Y_2W_3O_{12}$ with perovskite structures, the overall TEC of the composite can be effectively lowered, which enhances the mechanical durability of the cathode during high-temperature operation of SOFCs [29,30]. Various perovskite-NTE material combinations have been developed, showing significant success in reducing TEC while preserving catalytic efficiency. For instance, PBSC/SZM [31], SNC/SZM [32], BSF/NM [33], LSCF/SZM [34], etc., have demonstrated substantial improvements in thermal stability without compromising ORR performance. Despite these advances, challenges persist in optimizing these combinations, particularly in selecting the right perovskite-NTE pairs and managing the delicate balance between TEC reduction and catalytic activity, which is essential for maintaining the overall efficiency of SOFCs.

Scandium tungstate ($Sc_2W_3O_{12}$, ScWO), a member of the $A_2W_3O_{12}$ family of materials, has not been previously explored in SOFC composite cathodes. This study investigates the potential of ScWO as an NTE material when combined with BSCF, building on the established benefits of $A_2W_3O_{12}$-type compounds such as $Y_2W_3O_{12}$ (YWO) for improving thermal expansion characteristics. YWO has been shown to effectively reduce the TEC of perovskite cathodes while maintaining electrochemical stability. In this work, ScWO was selected to examine the impact of varying the A-site cation type and size within NTE materials on the performance of composite cathodes. Specifically, we aimed to assess how these variations affect thermal and electrochemical properties, particularly in mitigating cobalt reduction in the BSCF matrix at high temperatures. To achieve this, we designed BSCF/ScWO composite cathodes that incorporate a thermal expansion offset strategy, along with cobalt reduction suppression. The thermal expansion offset strategy directly improves thermal compatibility between the cathode and the electrolyte, while the interaction between BSCF and ScWO mitigates cobalt reduction. This interaction enables scandium to occupy the B-site of BSCF, thereby reducing cobalt reduction at elevated temperatures. We investigated the microstructural evolution of the composite cathode and the cathode/electrolyte interface after thermal cycling between 600 °C and 300 °C to validate the effectiveness of this strategy. Furthermore, we explore the trade-off between catalytic activity and stability, emphasizing the crucial role of NTE material selection and A-site cation interactions in enhancing the performance and durability of SOFCs.

2. Experimental

2.1. Sample synthesis

In this study, five distinct variants of cathodes were synthesized to tailor their thermal expansion properties. These included BSCF and its composites with $Sc_2W_3O_{12}$ (ScWO) in various mass ratios and sintering conditions. The variants synthesized are.

1. BS10-950: BSCF with 10 wt% ScWO, calcined at 950 °C
2. BS10-800: BSCF with 10 wt% ScWO, calcined at 800 °C
3. BS20-950: BSCF with 20 wt% ScWO, calcined at 950 °C
4. BS20-800: BSCF with 20 wt% ScWO, calcined at 800 °C

Phase-pure $Ba_{0.5}Sr_{0.5}Co_{0.8}Fe_{0.2}O_{3-\delta}$ (BSCF) powder was synthesized via the sol-gel method. Stoichiometric amounts of nitrates were dissolved in water, with EDTA and citric acid used as complexing agents. Ammonia solution was added to maintain the pH. The solution was mildly heated to induce gelation, and the resulting gel was heated at 250 °C for 12 h to remove organics. The obtained powder was then calcined at 950 °C for 2 h in air. The NTE material $Sc_2W_3O_{12}$ was prepared using a solid-state reaction route. Ethanol was added to an appropriate amount of Sc_2O_3 and WO_3, and the mixture was ball-milled for 10 h at 300 RPM. After air-drying in an oven at 80 °C, the mixture was calcined at 600 °C for 6 h, then at 1000 °C for 6 h in air. Commercialized $Sm_{0.2}Ce_{0.8}O_{1.9}$ (SDC) was used as the electrolyte material to prepare electrolyte discs. Appropriate amounts of BSCF and $Sc_2W_3O_{12}$ were mixed with a mortar and calcined at 950 °C for 2 h in the air to produce a composite cathode.

2.2. Fabrication of fuel cells

Electrolyte pellets, 495 μm thick and 11 mm in diameter, were prepared using SDC, which was dry pressed at 4 MPa and calcined at 1450 °C for 7 h in the air. Composite cathode powder was dispersed in isopropyl alcohol (IPA) and glycerol and then ball-milled at 300 RPM for 2 h to produce a cathode slurry. This slurry was sprayed on both sides of the electrolyte disc, followed by calcination at 950 °C for 2 h in the air to achieve a symmetric cell configuration: cathode/electrolyte/cathode.

2.3. Characterizations

The crystal structure of the synthesized composite cathode powder was characterized by X-ray diffraction (XRD) using a Bruker D8-Advanced X-ray diffractometer with nickel-filtered Cu-Kα radiation. Samples were scanned at 40 kV and 40 mA over an angle range of $2\theta = 10°–90°$, with a step increment of 0.1°. X-ray photoelectron spectroscopy (XPS) was conducted using a Kratos Axis Ultra spectrometer with AlKα (1486.8 eV) radiation at 150 W to analyze surface chemistry. Data were processed using CASAII software. Dense rectangular bar-shaped samples were formed by dry-pressing the synthesized powders and firing at 1200 °C for 5 h for BSCF and composite cathodes at 1150 °C for 20 h in air to observe thermal expansion. The thermal expansion coefficient (TEC) measurements were performed using the NETZSCH TMA 402 F3 instrument, tested in the temperature range of RT-800 °C under an air environment. The initial densities of the sintered specimens were determined using the Archimedes method in distilled water at room temperature (density assumed as 1.0 g/cm^3) [35]. The measured density was 5.51 g/cm^3 for BSCF, corresponding to a relative density of approximately 96.40 %. The BS10-950 sample showed a density of 5.38 g/cm^3, corresponding to a relative density of approximately 97.53 %. These values indicate adequate densification suitable for reliable dilatometry analysis.

The temperature-programmed desorption (TPD) of oxygen was assessed using a Micromeritics AutoChem II & HP apparatus. Samples were reduced in pure helium (50 mL/min), and TCD signals were recorded from 50 to 800 °C under a helium flow. Thermal analysis of the electrode material was performed using thermogravimetric analysis (TGA) with a Q50 instrument at a heating rate of 10 °C/min under flowing air (20 mL/min), from room temperature up to 800 °C.

Surface morphology and the cathode/electrolyte interface were examined before and after a durability test using scanning electron microscopy (SEM) with a JEOL 7100 instrument. Transmission electron microscopy (TEM) imaging was performed using a field emission transmission electron microscope (HF5000) equipped with energy-dispersive X-ray spectroscopy (EDS) capabilities. Samples for TEM were prepared using an ethanol dispersion method and mounted on a copper grid. For SEM-EDS analysis, composite pellets were prepared and analyzed using a Hitachi SU3500 with a 20 kV accelerating voltage. TEM lamellae from the composite cathode pallet cross-section were also tested using the HF5000.

2.4. Electrochemical test

Electrochemical impedance spectroscopy (EIS) was employed to measure the polarization resistance (Rp) of symmetrical cells using a PGSTAT302 autolab workstation. The EIS measurements were performed over a frequency range of 10,000 Hz–0.1 Hz at temperatures between 500 and 700 °C, with air as the oxidant at a consistent flow rate of 150 mL/min. The Rp values were extracted from the EIS spectra by calculating the difference between the high- and low-frequency intercepts on the real axis. Silver paste served as the current collector, with silver wires used to connect the cells to the external circuit.

2.5. Durability test

To evaluate the thermal stability and cycling resistance of the cathode materials, we conducted 40 thermal cycles between 600 °C and 300 °C. ASR measurements were taken every 10 cycles to assess the impact of thermal cycling on the material's electrochemical performance.

Focused ion beam-scanning electron microscopy (FIB-SEM) was employed to analyze microstructural changes in BSCF and BS10-950 electrode materials caused by thermal cycling. The symmetric cells using both electrodes BSCF and BS10-950 were subjected to 100 thermal cycles between 600 °C and 300 °C, mimicking operational stress. For the FIB-SEM analysis, regions with dimensions of 20 μm by 20 μm were selected, with a slice thickness of 50 nm, resulting in an analysis volume of 20 μm^3. For 3D reconstruction using Amira software, the selected regions had volumes ranging from 0.047 μm^3 to 0.058 μm^3. This selection ensured consistency across samples and minimized potential misalignment during the volumetric imaging process. The analysis allowed for the quantification of porosity changes before and after thermal cycling, providing crucial insights into the structural stability of the electrode materials.

3. Result and discussion

In our study, we synthesized and analyzed five distinct variants of $Ba_{0.5}Sr_{0.5}Co_{0.8}Fe_{0.2}O_{3\text{-}\delta}$ (BSCF) and its composites with $Sc_2W_3O_{12}$ (ScWO) in various mass ratios and sintering conditions. These included BS10-950, BS10-800, BS20-950, and BS20-800, as described in the Experimental section. The variations were intended to explore how different synthesis conditions affect the microstructure, composition, and thermal expansion behaviour of the cathodes, to identify the optimal variant for further thermal cycling and stability analysis. Fig. 1a illustrates the schematic mechanism underlying the study, showing that the composite cathode maintains its structural integrity even after frequent thermal cycling, in contrast to pure BSCF. This enhanced stability is attributed to the reduction in TEC resulting from the dilution of Co^{+2} valency due to incorporating ScWO (NTE material) in the BSCF matrix. The interaction between ScWO and BSCF helps mitigate phase separation, improving the composite's durability and performance under thermal cycling.

Initial analysis of the crystallographic structure of the cathode variants was conducted using X-ray diffraction (XRD). The diffraction patterns provided insights into phase composition, potential secondary phases, and crystal lattice parameters. The XRD data revealed structural modifications resulting from incorporating ScWO into the BSCF matrix. Fig. 1b shows the XRD patterns for BSCF, ScWO, and the composite cathode BS10-950. Our methodology accurately reproduced the XRD patterns documented in the literature for both BSCF and ScWO [36,37]. The XRD spectra exhibited characteristic peaks consistent with the expected crystallographic structures of BSCF and ScWO, confirming the reliability of our synthesis protocol. Notably, the BS10-950 composite showed minor impurity peaks, suggesting chemical interactions between BSCF and ScWO components. The impurity phase observed between 25° and 50° in Fig. 1b is identified as $BSWO_4$, as confirmed by comparison with data from the Crystallography Open Database (COD). This phase indicates the formation of an interphase between the BSCF and ScWO phases during the sintering process. The presence of this interphase enhances the stability and structural integrity of the composite, aligning with previous studies on NTE perovskites [29,30]. Moreover, the formation of the $BSWO_4$ interphase results in the dilution of ScWO, which is evident as a weakening of the ScWO peak in the XRD pattern.

This is essential to ensure strong chemical bonds between the materials and prevent phase separation during processing steps such as sintering, testing, or thermal cycling [29]. Such chemical interconnections enhance the integrity and stability of the composite cathode's crystal structure.

Further analysis of the XRD data for various composites is presented in Figs. S1 and S2, where the patterns for BSCF, BS10-800, BS20-800, BS10-950, and BS20-950 are shown, with a zoomed-in view of the main peaks to highlight the variations in peak positions and intensities (Fig. S2). These differences provide insight into the structural modifications that occur due to variations in sintering temperature and ScWO content. Additionally, Figs. S3 and S4 compare the XRD patterns for BSCF, BY10, and BY20 composites, further illustrating the structural changes when using YWO as the NTE material. These comparisons are crucial for understanding how different NTE materials impact the structural integrity of the cathode materials.

Due to the significant difference in thermal expansion coefficients (TEC) between ScWO and BSCF, delamination between the two phases can occur easily during thermal cycling if they are only physically connected. A chemical reaction between the two materials creates a strong connection between the phases, ensuring mechanical integrity. As shown in Fig. 1c BS10-950, the incorporation of ScWO into BSCF significantly reduced the TEC of the composite cathode from $20.92 \times 10^{-6}\ K^{-1}$ to $13.67 \times 10^{-6}\ K^{-1}$ for RT-800 °C. This reduction in TEC is crucial for improving the thermo-mechanical compatibility of the cathode with other components in SOFCs, thus reducing the risk of delamination and enhancing overall structural stability during thermal cycling.

Although the characteristic peak of ScWO was not present, the persistence of the ScWO phase was confirmed by other methods described in the following sections. The presence of B-site Sc in the BSCF phase after calcination is supported by SEM-EDS results discussed later.

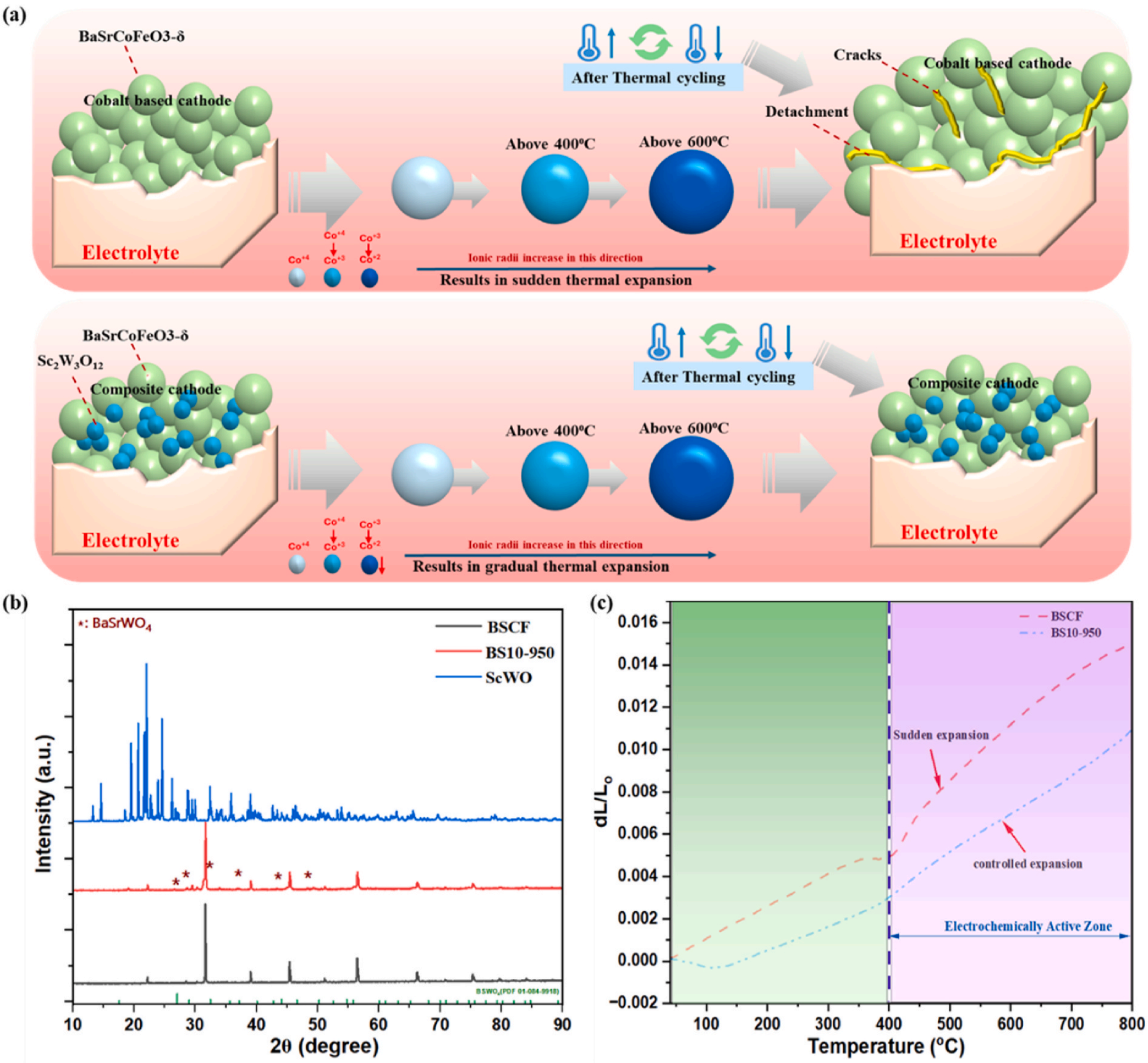

Fig. 1. (a) Schematic of effect of integration of ScWO into BSCF structure, (b) XRD patterns of BSCF, ScWO and BS10-950, (c) TEC profiles for dense pallets of BSCF and BS10-950 electrode in RT-800 °C in air.

Therefore, after calcination of the ScWO/BSCF mixture, the resulting BS10-950 composite consists of newly formed interfacial BSWO, residual ScWO, and Sc-occupied BSCF.

To validate our hypothesis that A-site cations from BSCF react with ScWO to form $BSWO_4$ and that Sc diffuses into the B-site of BSCF to create a Sc-doped BSCF perovskite structure, we employed high-resolution transmission electron microscopy (HR-TEM). As shown in Fig. 2b and c, HR-TEM confirms the presence of ScWO, $BSWO_4$, and Sc-doped BSCF phases within the BS10-950 composite. The lattice spacing measurements from a selected region in Fig. 2a demonstrate the coexistence of these phases. The observed lattice spacings, d(011) = 2.81 Å (PDF 00-055-0563), d(204) = 2.05 Å (PDF 01-084-9918), and d(213) = 3.09 Å (PDF 01-078-8209), correspond to the BSCF perovskite, $BSWO_4$, and ScWO phases, respectively. These lattice spacings are consistent with the peaks observed in the XRD data.

To further substantiate the interface formation and Sc diffusion into the BSCF structure, we conducted elemental distribution mapping of the BS10-950 pellet. To ensure a smooth surface for energy-dispersive X-ray spectroscopy (EDS) analysis, the pellet was sintered at high temperature to achieve densification. SEM-EDS has been used in this study to cover a larger cross-sectional area of the sample, ensuring a more representative elemental distribution across the composite cathode.

As depicted in Fig. 2d, the area marked with a circle represents the $BSWO_4$ phase, while the area marked with a rectangle denotes the BSCF matrix where scandium is uniformly distributed. In the circular region, the intensities of Ba, Sr, and W are higher, indicating that this area corresponds to the $BSWO_4$ phase. To gain a deeper understanding, we performed point analysis by selecting three points in each region and plotted the average elemental composition in Fig. 2c. The results show that the circular region is tungsten-rich, whereas the rectangular region has a higher concentration of scandium. Similar findings from a line scan across the circular to rectangular regions are presented in Supplementary Fig. S6. Additionally, EDS analysis confirmed the presence of all expected elements, supporting our observations of interface formation and elemental distribution in the composite structure. The EDS mapping of the Co element in Fig. 2d shows localized variations in the cobalt distribution, which can be attributed to phase interactions and local chemical environment changes within the composite. The few dark dots observed do not represent cobalt segregation but reflect minor variations in the material's structure. These observations are consistent with the expected behaviour of composite materials and do not impact the overall integrity of the cathode.

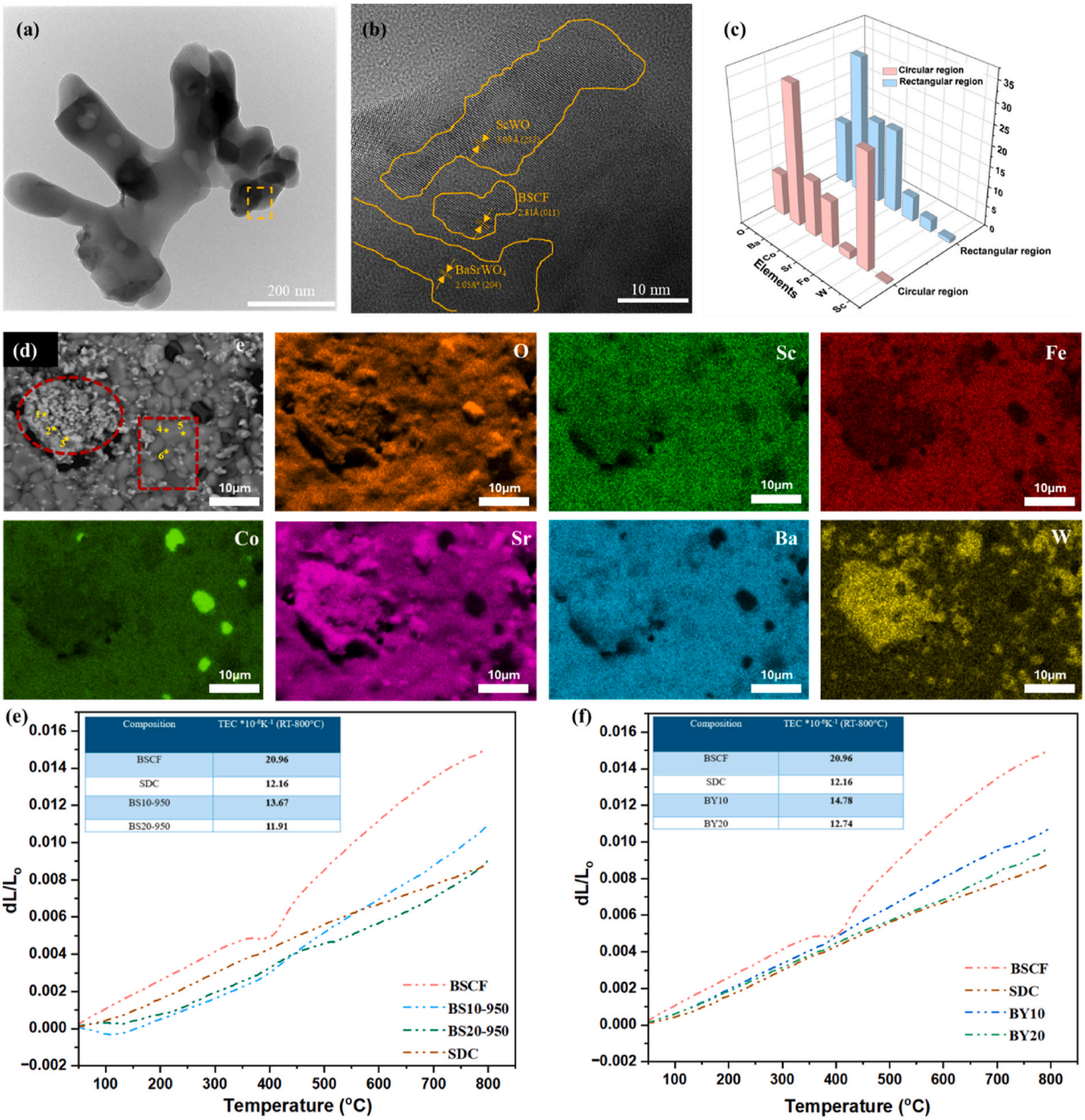

Composition	TEC $*10^{-6}K^{-1}$ (RT-800°C)
BSCF	20.96
SDC	12.16
BS10-950	13.67
BS20-950	11.91

Composition	TEC $*10^{-6}K^{-1}$ (RT-800°C)
BSCF	20.96
SDC	12.16
BY10	14.78
BY20	12.74

Fig. 2. (a)HRTEM image of BS10-950 electrode, (b)HRTEM image for the coexistence of ScWO, BaSrWO, and Sc-doped BSCF, (c)Average elemental composition of marked region fin Fig. 4d e^- image, (d) SEM-EDS analysis for BS10-950 electrode, (e) TEC profiles for dense pallets of BSCF, SDC, BS10-950, and BS20-950 electrode in RT-800 °C in air, (f) TEC profiles for dense pallets of BSCF, SDC, BY10, and BY20 electrode in RT-800 °C in air.

Fig. 2e and f further explore the impact of incorporating different NTE materials on the TEC profiles of BSCF composites. Fig. 2e shows the TEC profiles for BSCF and composites with 10 % and 20 % ScWO, while Fig. 2f presents the TEC profiles for BSCF and composites with 10 % and 20 % YWO.

The data demonstrate that both YWO and ScWO effectively lower the TEC of BSCF, with the extent of this reduction being influenced by the concentration and type of the negative thermal expansion (NTE) material used. Existing literature indicates that increasing the size of the A-site cation in NTE materials further decreases the TEC [38]. While in perovskite structures, an increase in the size of the B-site cation typically results in a higher TEC, primarily due to its influence on spin state transitions under SOFC operating conditions [39,40]. This trend is evident in the TEC values for the variants with 10 % and 20 % loading of ScWO and YWO: BY10, BY20, BS10-950, and BS20-950, where the TEC values are 14.78 × 10^{-6} K^{-1}, 12.74 × 10^{-6} K^{-1}, 13.67 × 10^{-6} K^{-1}, and 11.91 × 10^{-6} K^{-1}, respectively. Notably, Sc occupancy at the B-site of BSCF results in a more significant reduction in TEC, despite ScWO having a higher intrinsic TEC than YWO in the RT-800 °C range, with TEC values of -4.21×10^{-6} K^{-1} for ScWO and -7.2×10^{-6} K^{-1} for YWO. The significant reduction in TEC observed with ScWO might not be due to the formation of $BaSrWO_4$, as the interface formation of $BaSrWO_4$ occurs in both YWO and ScWO cases. YWO (-7.2×10^{-6} K^{-1}) has a more negative effect on TEC than ScWO (-4.21×10^{-6} K^{-1}). However, adding 10 % ScWO results in a more significant reduction in TEC, likely due to the unique interaction between Sc and the B-site of the BSCF matrix. This interaction helps reduce the TEC further by facilitating the presence of the NTE phase, while minimizing the dilution of the perovskite phase. These factors work together to achieve enhanced thermal expansion properties in the ScWO case.

The B-site occupancy of Sc reduces the TEC and restricts lattice oxygen release, affecting the overall oxygen reduction reaction (ORR) process. This complex interplay between TEC reduction and ORR performance highlights the importance of selecting the appropriate NTE material and optimizing its concentration to achieve a balance between thermo-mechanical compatibility and electrochemical performance in SOFC cathodes.

To investigate the effect of scandium (Sc) doping on the chemical states of B-site elements in BS10-950, X-ray photoelectron spectroscopy (XPS) was conducted. The deconvoluted spectra of Co 2p region is presented in Fig. 3a. From Fig. 3a, it can be interpreted that the significant modifications in the chemical state of cobalt (Co) in the BS10-950 sample are seen when compared to the reference BSCF. Furthermore, the XPS spectra in the Fe 2p region showed reduced peak intensity with a concomitant shift in binding energy value toward the lower B.E. region, exemplifying the dilution in Fe content and might be due to the change in the oxidation state of Fe due to Sc-occupancy at B-site of perovskite structure (Supporting Information, Fig. S8).

Deconvolution of the XPS spectra in Ba 3d/Co2p region in BSCF reveals distinct cobalt oxidation states. In BSCF, both Co^{3+} and Co^{4+} are found to coexist in the sample with binding energy value 779.48 and 794.66 eV, 780.61 and 796.18 eV, respectively. The Co 2p XPS data exhibits binding energy values closely aligned with the reference values, indicating a consistent electronic environment and oxidation state for

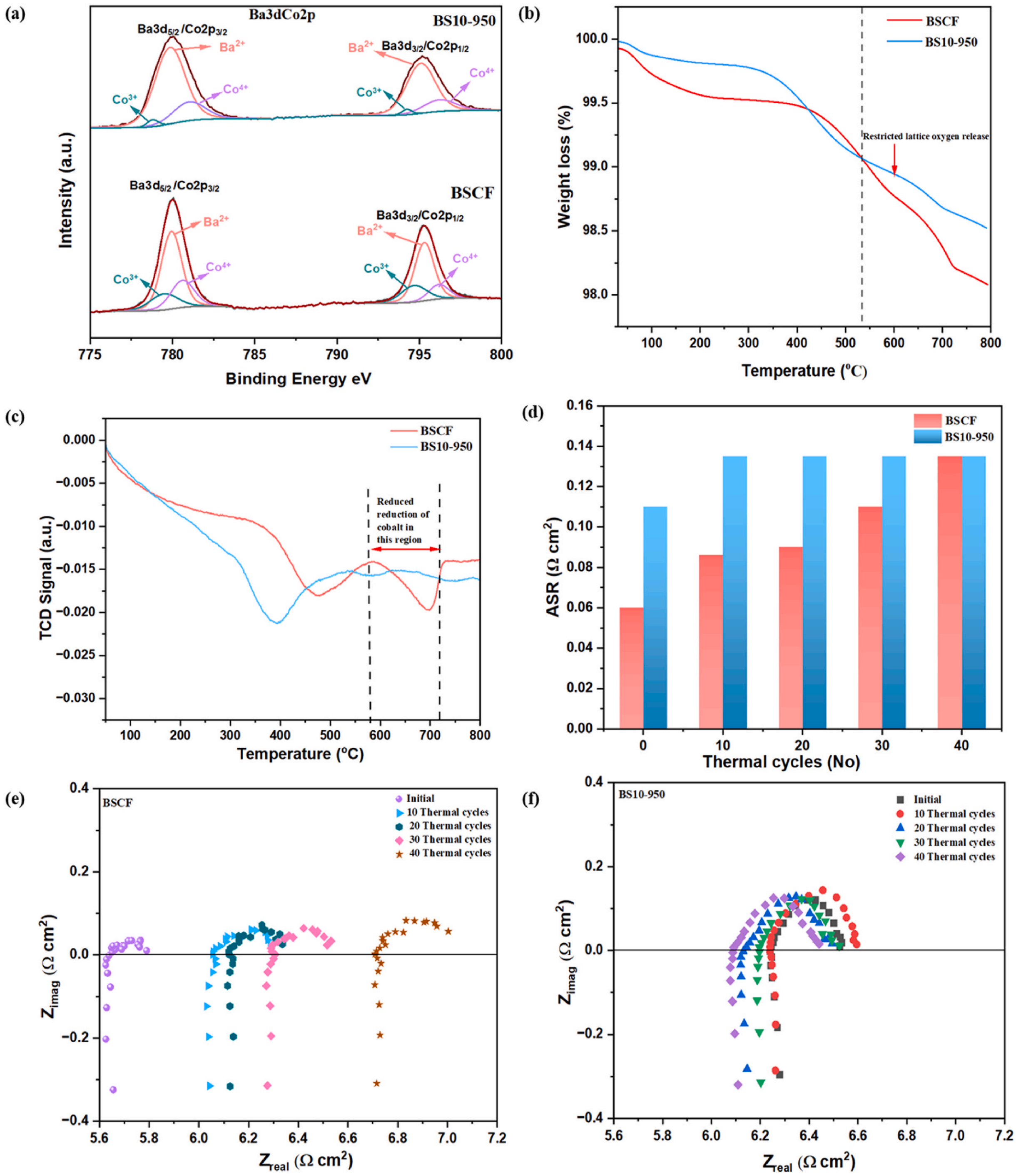

Fig. 3. (a) XPS profiles of Co2p for BSCF and BS10-950, (b) TGA curve for BSCF and BS10-950 cathode powder, (C) O_2-TPD profiles for BSCF and BS10-950 cathode powder, (d) effect of thermal cycling on ASR values for BSCF and BS10-950 symmetric cells, EIS Nyquist plot for BSCF (e), and BS10-950 (f) after 40 thermal cycling.

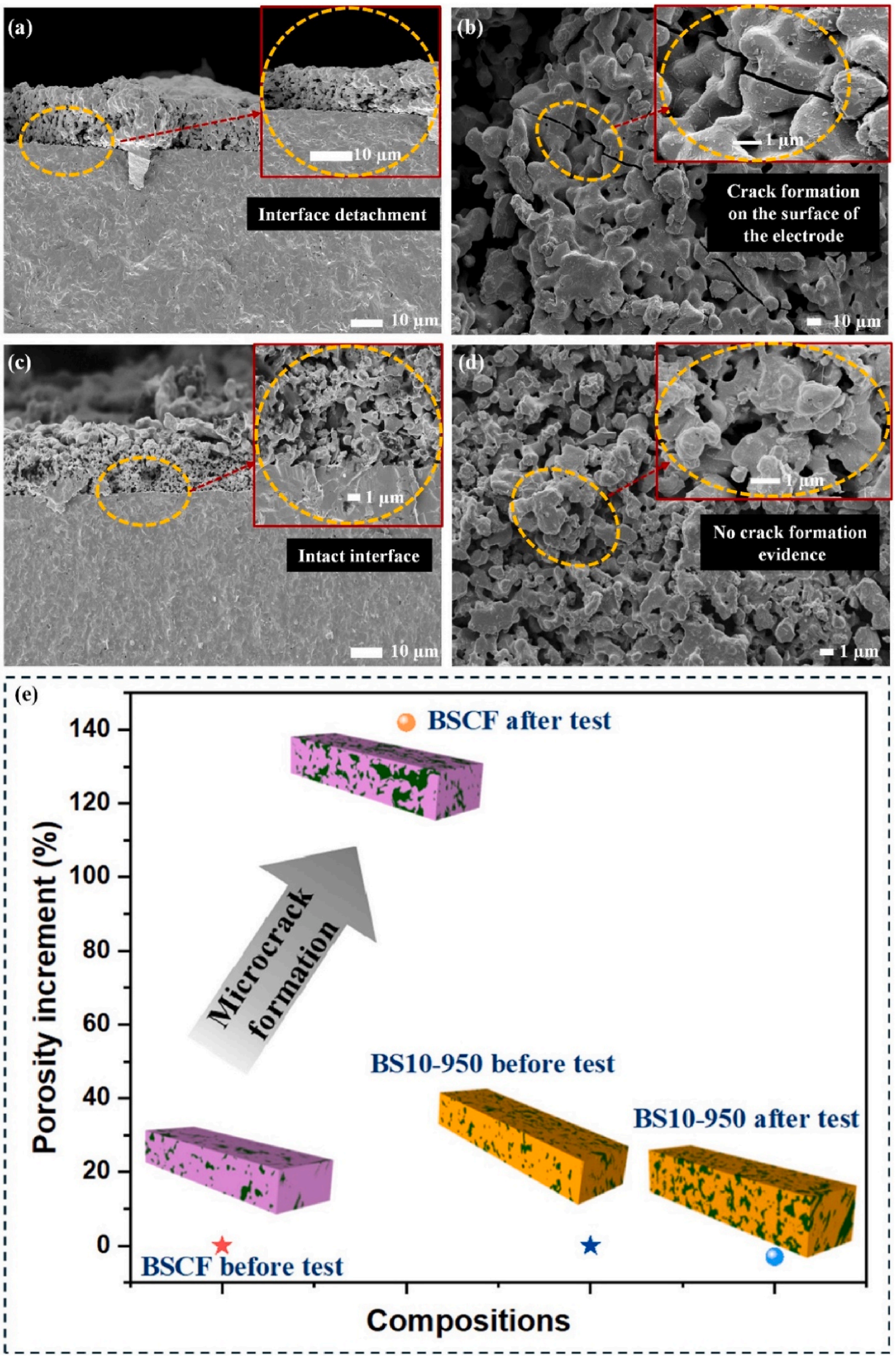

Fig. 4. After the durability test (40 thermal cycling), SEM images (a) cross-section of the interface of electrode/electrolyte for BSCF, (b) surface analysis of BSCF, (c) cross-section of the interface of electrode/electrolyte for BS10-950, (d) surface analysis of BS10-950, (e) FIB analysis before and after the durability test (100 thermal cycling) for BSCF and BS10-950.

cobalt within the BSCF sample [36].

In contrast, deconvoluted XPS spectra of BS10-950 in Ba3d/Co2p show the occurrence of predominantly Co^{4+} oxidation state at 781.01 eV and 796.23 eV. At the same time, the peaks corresponding to Co^{3+} are significantly weak at 778.80 eV and 794.23 eV, denoting the low existence of this oxidation state in the sample. The reason for a lower

Table 1
Deconvoluted results for Co2p XPS spectra for BSCF and BS10-950.

Cathode materials	Element	Binding Energy(eV) $Co2p_{3/2}$	$Co2p_{3/2}$ (% concentration)	Binding Energy(eV) $Co2p_{1/2}$	$Co2p_{1/2}$ (% concentration)
BSCF	Co^{4+}	780.61	14.26 ± 1.43 %	796.18	6.48 ± 0.65 %
BSCF	Co^{3+}	779.48	9.95 ± 0.99 %	794.66	9.36 ± 0.94 %
BS10–950	Co^{4+}	781.01	12.42 ± 1.24 %	796.23	7.68 ± 0.77 %
BS10–950	Co^{3+}	778.80	1.64 ± 0.16 %	794.23	1.09 ± 0.11 %

oxidation state of Co^{3+} and Co^{2+} might suggest that the Sc occupancy at the B-site and its interaction in BS10-950 influence the overall Co oxidation state/distribution. The interaction of Sc in BSCF plays a crucial role in stabilizing these oxidation states (as shown in Table 1).

Further insights come from the O 1s XPS profile (Supporting Information, Fig. S9), showing a marked reduction in oxygen vacancies in BS10-950 compared to BSCF, consistent with our thermal gravimetric analysis (TGA)(Fig. 3b) and temperature-programmed desorption (TPD) results, which indicate less lattice oxygen release and cobalt reduction in BS10-950 above 500 °C. Though we acknowledge that O 1s XPS does not directly determine the oxygen vacancy content; however, it can be used to quantify the oxygen vacancy concentration as oxygen vacancies are typically the most dominant defect in materials such as perovskites and fluorite oxides [41]. These changes in Co valency and oxygen vacancy concentration directly influence the electrochemical performance of the composite cathode by stabilizing the TEC. The slight shift in O1s binding energy for BS10-950 compared to BSCF can be attributed to changes in the local chemical environment and electronic interactions caused by the Sc occupancy at the B-site of BSCF and interaction between BSCF and ScWO phases. Detailed component concentrations for O1s are provided in the Supporting Information Table S1. The reduction in Co^{2+}, which has a larger ionic radius, helps to control TEC, minimizing thermal expansion mismatches.

X-ray diffraction (XRD) analysis confirms the formation of the $BSWO_4$ phase in BS10-950, a cobalt-free phase critical in reducing the overall TEC. As shown in Fig. 3c, oxygen temperature-programmed desorption (O_2-TPD) was conducted to investigate the oxygen desorption behaviour and the reducibility of B-site cations, which influence chemical expansion. The O_2-TPD profile reveals two distinct desorption peaks: one at lower temperatures (300–600 °C) and another at higher temperatures (above 600 °C). The lower temperature peak is associated with the reduction of Co^{4+} and/or Fe^{4+} to Co^{3+} and/or Fe^{3+}, while the high-temperature peak corresponds to the further reduction of Co^{3+} to Co^{2+} [42]. Notably, the reference material, BSCF, exhibits a significantly higher intensity at the high-temperature peak, indicating an increased tendency of Co^{3+} to reduce to Co^{2+}. This higher Co^{2+} concentration, with its larger ionic radius relative to Co^{4+} and Co^{3+}, likely contributes to the expanded TEC observed in BSCF. In contrast, the lower intensity of the high-temperature peak in BS10-950 indicates a reduced formation of Co^{2+}, which supports the lower TEC of the material. The reduction in chemical expansion is further supported by the restricted lattice oxygen release observed in the composite cathode BS10-950, indicating a limited formation of oxygen vacancies. This finding is confirmed by the O1s XPS spectra presented in the supporting information Figure S9, which confirms a lower concentration of oxygen vacancies in BS10-950 than the reference BSCF material. The reduction in TEC and chemical expansion contributes to the material's enhanced structural stability under operational conditions. Furthermore, the reduced oxygen vacancy concentration observed in the O 1s XPS profile (Supporting Information, Fig. S9), along with the suppressed lattice oxygen release and cobalt reduction behaviour above 500 °C (as shown in TGA and TPD results), may not solely reflect intrinsic changes in BS10-950. These differences could also be significantly influenced by the dilution effect introduced by the composite formulation. This dilution may limit the extent of electrochemical activity of the active phase, thereby contributing to the observed decrease in reducibility and oxygen loss.

To assess thermo-mechanical durability, we subjected the electrodes to thermal cycling, measuring area-specific resistance (ASR) every 10 cycles (Fig. 3d). BS10-950 exhibited only a minor ASR increase from 0.11 to 0.13 Ω cm^2 after 40 cycles, an 18 % rise, mostly occurring in the initial 10 cycles. In stark contrast, BSCF's ASR surged from 0.060 to 0.13 Ω cm^2, a 116 % increase, indicating severe degradation. Electrochemical impedance spectroscopy (EIS) Nyquist plots (Fig. 3e–f) further highlight BS10-950's enhanced durability, with BSCF showing significant Ohmic resistance growth due to electrode-electrolyte delamination during cycling. To further support the ASR degradation trends shown in Fig. 3d, a plot of ohmic resistance versus thermal cycle number has been included in the Supporting Information (Fig. S18). This figure reveals that the rate of increase in ohmic resistance for BSCF is significantly higher than for BS10-950, highlighting the superior interfacial and structural stability of the composite under repeated thermal cycling. The BS10-950 composite electrode initially shows a higher ohmic resistance compared to pristine BSCF, as observed in the EIS Nyquist plots (Fig. 3e–f). This difference can be attributed to the lower electronic conductivity of BS10-950, resulting from the reduced BSCF content and the presence of less conductive phases such as $BSWO_4$. However, this slight drawback is effectively balanced by the composite's enhanced structural integrity during thermal cycling. These results demonstrate that BS10-950 maintains superior thermo-mechanical stability and confirms its effectiveness for demanding high-temperature applications requiring both durability and strong electrochemical performance.

The morphological analysis of the two electrodes after thermal cycling (Fig. 4a, b, 4c, and 4d) reveals significant differences. The BSCF electrode exhibited visible cracks both at the electrode-electrolyte interface and throughout the electrode itself, indicating considerable thermal stress and mechanical degradation. These cracks can severely impair electrochemical activity and ion transport, compromising the fuel cell's performance and long-term durability. In contrast, the BS10-950 electrode showed no signs of cracking, highlighting its superior thermo-mechanical stability and durability. This stability is crucial for maintaining consistent performance over prolonged operations. The absence of cracks suggests a higher resistance to thermal cycling-induced stress, likely due to the optimized calcination temperature and the presence of the $BSWO_4$ phase, which enhances structural integrity and promotes better stress distribution.

Supporting Information Figures S7 a and b provide SEM analysis of the BS10-950 electrode after a 200-h stability test, showing an intact interface between the cathode and electrolyte. This observation further confirms the structural integrity of the BS10-950 electrode and the benefits of using a thermally stable composite cathode. Both the BSCF and BS10-950 electrodes used in these tests had similar thicknesses, with the BSCF cathode measuring 12.28 μm and the BS10-950 cathode measuring 13.62 μm for the durability test, and 17 μm for the stability test. The enhanced durability of the BS10-950 electrode ensures sustained electrochemical activity and efficiency, making it a more suitable choice for applications where frequent temperature fluctuations are anticipated. The observed microstructural degradation in BSCF after thermal cycling was further substantiated through advanced imaging techniques. While conventional Scanning Electron Microscopy (SEM) provided initial insights, the potential for artifacts introduced during sample preparation necessitated a more precise approach. Employing Focused Ion Beam-Scanning Electron Microscopy (FIB-SEM) for three-dimensional (3D) reconstruction allowed for a more accurate assessment of the microstructural changes.

Fig. 4e presents the FIB-SEM analysis and 3D reconstructions of BSCF and BS10-950 electrodes, both before and after 100 thermal cycles, revealing significant differences in their porosity behaviour. In this reconstruction, microcracks were categorized as porosity due to the difficulty in differentiating between pores and cracks. The BSCF electrode exhibited a significant increase in porosity, with a relative increment exceeding 140 %, suggesting extensive microcrack formation and a high susceptibility to thermal stress [43]. This observation aligns with the data shown in Fig. 3e, where the increase in ohmic and polarization resistance during thermal cycling strongly indicates delamination at the electrode/electrolyte interface and cracking within the electrode layer [44]. The formation of these cracks is primarily driven by prolonged exposure to high temperatures and frequent thermal cycling, as supported by previous studies [45,46]. Under typical SOFC operating conditions (600–1000 °C), multi-physics fields of stress can arise, contributing to crack nucleation and propagation in the electrode [47]. Thermal gradients during operation, coupled with reduction and oxidation processes, can generate residual mechanical stresses, potentially triggering electrode delamination or crack nucleation [48–53]. In BSCF, crack propagation is largely attributed to these factors. In contrast, the BS10-950 composite cathode exhibited superior structural stability, with no significant change in porosity after thermal cycling. This resilience suggests that the composite structure remained intact and resistant to thermal degradation, which can be attributed to its controlled thermal expansion and reduced thermal stress within the electrode and at the cathode/electrolyte interface. Thermal cycling resistance of the composite cathode is superior, likely due to the strong interphase bonding between $Sc_2W_3O_{12}$ and BSCF phases. Previous research has shown that composite cathodes with similar phases exhibit minimal phase transitions and enhanced stability during thermal cycling [29,30], supporting the improved thermal cycling resistance of our material. This enhanced stability is attributed to the synergistic effect between the negative thermal expansion property of ScWO and the interface interaction between ScWO and BSCF, which helps prevent strain accumulation and phase degradation under high-temperature conditions.

The performance of symmetric cells was evaluated to compare the oxygen reduction reaction (ORR) activity between the pristine BSCF cathode and the BS10-950 composite cathode. While the pristine BSCF cathode exhibits superior electrochemical performance due to its high ORR activity, the BS10-950 composite demonstrates a decline in performance, attributed to its slightly lower ORR activity. This deterioration is due to the reduction in chemical expansion, with less release of lattice oxygen and reduced reduction of cobalt to Co^{2+}, which helps control the TEC. Despite this minimal electrochemical performance reduction, the BS10-950 composite offers significant advantages in terms of thermal stability and long-term durability for practical applications in SOFCs.

The BS10-950 material was subjected to a 200-h stability test, maintaining almost consistent performance. The ability of BS10-950 to retain its structural integrity and electrochemical performance over extended periods highlights its suitability for actual applications. Fig. 5a presents the Arrhenius plot for polarization resistance plot, showing that while the BS10-950 composite has a slightly higher ASR compared to the pristine BSCF, it remains within an acceptable range for effective SOFC operation. At 600 °C, the ASR for BSCF is 0.06 ± 0.01 Ω cm^2, while for BS10-950, it is 0.1 ± 0.01 Ω cm^2. Also, The ASR for BS20-950 was measured at 600 °C is 0.26 ± 0.01 Ω cm^2, which is relatively high due to restricted chemical expansion, resulting in reduced ORR activity. Consequently, BS10-950 was selected as the optimal material for further study, owing to its superior performance in both thermal expansion and electrochemical properties. The EIS Nyquist plots for BS10-950 at 650 °C and 600 °C, shown in Fig. 5b, further illustrate its stable impedance characteristics across these temperatures.

Additionally, the temperature dependence of the ASR for BSCF and YWO composites is provided in Fig. S14. This data is critical for understanding the electrochemical performance and thermal stability of these materials under operating conditions. The ASR values for the BSCF-YWO composites are compared to those of the BSCF-ScWO composites, showing a similar trend in performance. Also, Fig. S16 presents the DRT analysis of BSCF, BS10-950, and BS20-950 samples on the SDC symmetrical cell at 600 °C. Based on the frequency distribution, the deconvoluted peaks are classified into three distinct regions: high frequency (HF, $>10^3$ Hz), intermediate frequency (IF, 10^3–2×10^2 Hz), and

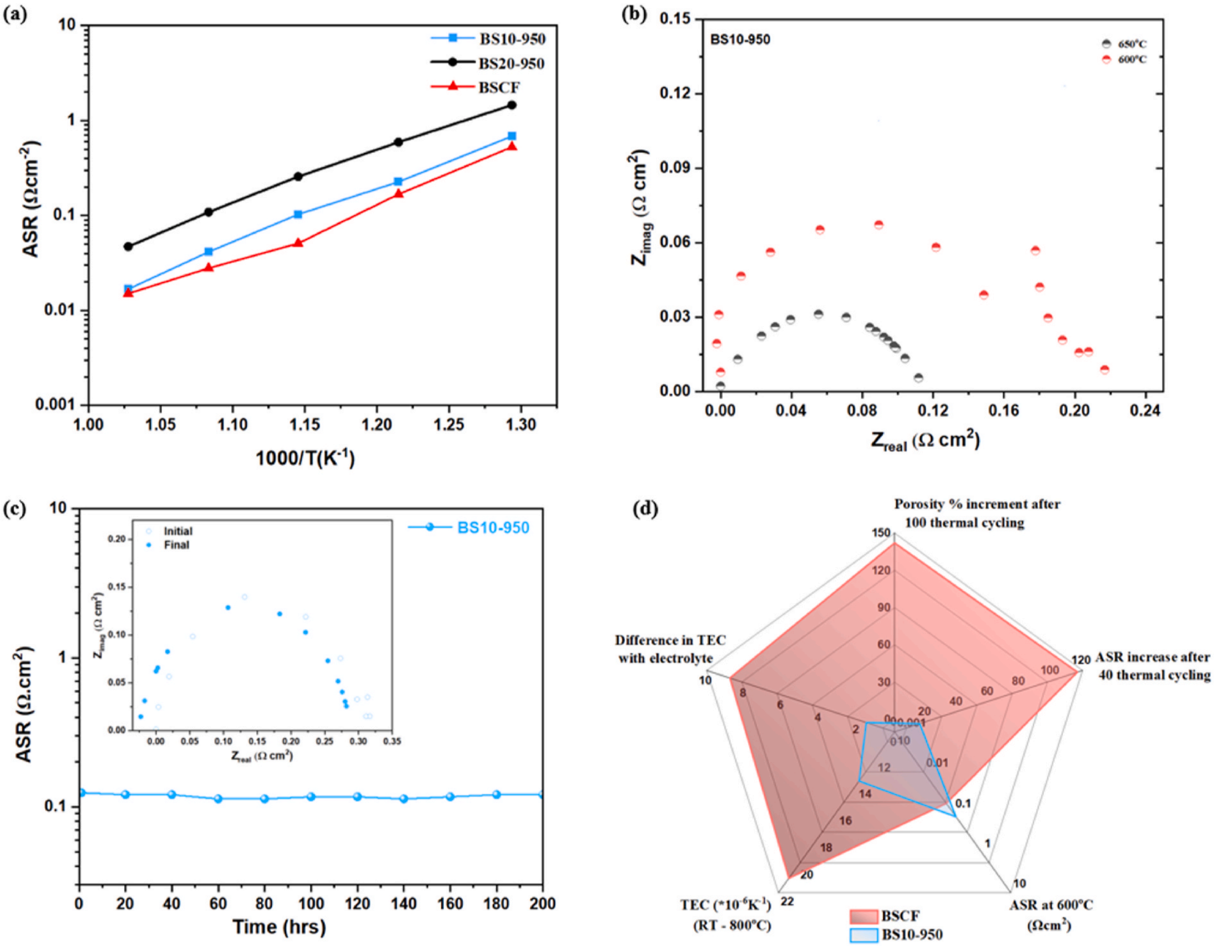

Fig. 5. (a) Arhenius plot for polarization resistance of BSCF and BS10-950, (b) EIS Nyquist plot for BS10-950 at 650 and 600 °C, (c) ASR presentation of 200hrs stability for BS10-950, (d) Spider web analysis for BSCF and BS10-950.

low frequency (LF, $<2 \times 10^2$ Hz). These regions correspond to different electrochemical processes: charge transfer and ion migration in the HF and IF regions, while the LF region is associated with surface exchange and surface mass transfer [54,55]. In the BS10-950 and BS20-950 samples, the decreased BSCF concentration reduces the ORR activity. With less BSCF in the electrode, the resistance in the HF and LF region primarily governs the total resistance, indicating that the charge transfer and ion migration on the air electrode significantly limit the electrocatalytic process. This analysis offers insights into the complex electrochemical behaviour of the composite cathodes, revealing the influence of material composition on ORR and related processes.

Moreover, the long-term stability test results, depicted in Fig. 5c, confirm that BS10-950 retains its performance with minimal degradation over 200 h. The ASR values at the start and end of the test are 0.12 Ω cm^2 and 0.12 Ω cm^2, respectively, showing a consistent performance. This confirmed the composite cathode's stability against prolonged thermal and thermomechanical stresses.

Integrating ScWO into BSCF results in a controlled reduction in cobalt oxidation states, leading to a decrease in TEC and enhanced thermomechanical stability. However, this also slightly affects ORR catalytic activity due to reduced oxygen vacancy concentration. Despite this, the composite cathode maintains an optimal balance, as the suppression of cobalt reduction prevents excessive lattice expansion while retaining sufficient ORR activity for practical SOFC applications.

The performance degradation observed in BS10-950 compared to the pristine BSCF can be linked to the BSCF dilution. However, this trade-off is balanced by the material's enhanced thermal stability and durability, which are critical for the longevity and efficiency of SOFC systems. The reduced cobalt reduction and limited chemical expansion in BS10-950, as evidenced by the TGA and TPD data, contribute to its stability, preventing the formation of detachment that could compromise performance.

To provide a comprehensive comparison between BSCF and the composite cathode BS10-950, a spider web analysis is presented in Fig. 5d, focusing on key thermal and electrochemical characteristics, including TEC values, thermal cycle resistance, microcrack formation, TEC mismatch between the electrolyte and cathode, and ASR values. These properties are specifically selected to highlight performance metrics where lower values correspond to improved material performance. The primary contribution of this study lies in the substantial reduction of the thermal expansion coefficient (TEC) achieved by incorporating ScWO into the BSCF matrix. The TEC was reduced from 20.92×10^{-6} K^{-1} to 13.67×10^{-6} K^{-1}, significantly enhancing the compatibility between the cathode and electrolyte, mitigating delamination risks, and improving thermo-mechanical stability under operational conditions. Furthermore, the composite cathode demonstrated enhanced resistance to thermal cycling and minimal microcrack formation, as confirmed by ASR measurements and microstructural analysis.

The performance of the BS10-950 composite cathode with only 10 % ScWO addition is comparable to or better than that of other recent composite cathodes reported in the literature([56,57]), which often require higher concentrations of secondary phases to achieve similar stability and performance. Despite the lower ScWO content, our material demonstrates excellent thermal cycling resistance and structural stability, highlighting the effectiveness of the ScWO-BSCF interaction in enhancing the cathode's overall performance with minimal additive content.

Additionally, to verify the effect of new phase formation, particularly through the interaction between BSCF and ScWO, on the electrical conductivity of the composite has been carefully examined. As shown in Fig. S17 (Supporting Information), the electrical conductivity of the BS10-950 composite, measured between 300 °C and 800 °C, increases gradually from 4.5 S cm^{-1} to 10.6 S cm^{-1}. In comparison, pure BSCF exhibits a higher conductivity, rising from 24 S cm^{-1} to 45 S cm^{-1} up to 500 °C before decreasing at higher temperatures. The conductivity data for pure BSCF closely match values reported in previous literature, confirming the reliability of our results. Although the BS10-950 composite exhibits lower intrinsic electrical conductivity compared to pristine BSCF, this does not directly translate to higher ASR values. ASR is influenced not only by electronic conductivity but also by interfacial resistance and electrode structural stability. Although the BS10-950 composite exhibits lower intrinsic electrical conductivity compared to pristine BSCF, this does not directly translate to higher ASR values. ASR is influenced not only by electronic conductivity but also by interfacial resistance and electrode structural stability. The BSCF electrode undergoes severe microstructural degradation during thermal cycling, including the formation of cracks and delamination at the electrode/electrolyte interface, which significantly increases its resistance. In contrast, the BS10-950 composite retains structural and interfacial integrity throughout cycling, maintaining stable contact with the electrolyte. This superior mechanical compatibility compensates for its lower conductivity, resulting in comparable or even more stable ASR performance over time.

The decrease in conductivity for the BS10-950 composite can be attributed to the dilution effect of ScWO, which lowers the overall conductivity. However, the interaction between BSCF and ScWO leads to Sc doping within the BSCF lattice, resulting in the formation of new phases that influence the composite's conductivity behaviour. This change in conductivity is consistent with the expected effects of ScWO on the BSCF structure and its role in altering the composite's electronic and ionic transport properties.

This synergistic strategy of combining NTE materials with traditional cathode structures is not limited to BSCF but can be applied to other high-performance cathode materials that face challenges related to high TEC and electrode/electrolyte incompatibility. By enhancing thermal stability and providing valuable insights into the optimal pairing of NTE materials with perovskites, this approach presents a flexible and effective strategy to improve the performance of a wide range of cathode materials in SOFCs.

4. Conclusion

This study demonstrated a synergistic strategy by integrating NTE ScWO with BSCF cathodes, resulting in significant improvement in thermal expansion properties and enhanced thermo-mechanical stability during prolonged thermal cycling. Among the composite cathodes synthesized, BS10-950 exhibited the most promising performance, with a remarkable reduction in the TEC from 20.92×10^{-6} K^{-1} to 13.67×10^{-6} K^{-1}. This reduction ensures better compatibility with other solid oxide fuel cell (SOFC) components, thereby mitigating the delamination and structural failure under operational conditions. The formation of a Sc-occupied perovskite structure, $BSWO_4$ interphase formation, and reduction in Co^{2+} valency enhance the structural integrity of the composite. Thermal cycling tests and post-durability morphological analysis revealed that BS10-950 maintained its structural integrity and exhibited minimal degradation in ASR over 40 thermal cycles between 600 and 300^{o}C, emphasizing its thermo-mechanical stability. Despite a slight reduction in oxygen reduction reaction (ORR) activity compared to pristine BSCF, the strategy employed in this study combining the thermal expansion offset effect with the suppression of cobalt reduction proves highly effective in enhancing long-term durability. This approach minimizes chemical expansion and mechanical degradation by balancing thermal expansion and stabilizing the cobalt oxidation state under operational conditions. Our recently developed SrCoO3-based cathodes, such as SSTC [58], SSNC [59], SCTV [60], and SNTC [61], show excellent ORR, however, they suffer from the problem of high thermal expansion. By integrating these mechanisms, the strategy mitigates the adverse effects of thermal cycling, making it a versatile and promising solution for enhancing the performance of a wide range of cathode materials in SOFC applications, extending beyond BSCF-based cathodes.

CRediT authorship contribution statement

Nilam Shah: Validation, Data curation, Methodology, Writing – original draft, Formal analysis, Writing – review & editing, Investigation. **Tianjiu Zhu:** Formal analysis, Data curation. **Xiaoyong Xu:** Writing – review & editing, Methodology, Writing – original draft, Investigation, Project administration, Conceptualization, Supervision, Data curation. **Hao Wang:** Resources, Project administration, Writing – original draft, Funding acquisition, Writing – review & editing, Methodology. **Zhonghua Zhu:** Resources, Funding acquisition, Writing – review & editing, Project administration, Conceptualization, Supervision, Investigation, Writing – original draft, Methodology. **Lei Ge:** Writing – original draft, Methodology, Supervision, Resources, Conceptualization, Writing – review & editing, Project administration, Funding acquisition.

Declaration of competing interest

The authors declare that they have no known competing financial interests or personal relationships that could have appeared to influence the work reported in this paper.

Acknowledgment

We appreciate technical support from the Centre for Microscopy and Microanalysis (CMM) at the University of Queensland. N Shah would like to thank the RTP research scholarship from the University of Queensland. ZH Zhu and H Wang would like to thank the financial support from Australian Research Council Discovery Project DP200101397 and DP250102334. L Ge wants to thank the financial support from ARC Future Fellowship project FT220100166.

Appendix A. Supplementary data

Supplementary data to this article can be found online at https://doi.org/10.1016/j.jpowsour.2025.237832.

Data availability

Data will be made available on request.

References

[1] X. Xu, X. Han, Y. Zheng, W. Zhou, K. Davey, S.-Z. Qiao, Developing solid oxide cells for sustainable generation of chemicals, Chem Catal. 3 (11) (2023) 100794, https://doi.org/10.1016/j.checat.2023.100794.

[2] E.P. Murray, T. Tsai, S.A. Barnett, A direct-methane fuel cell with a ceria-based anode, Nature 400 (6745) (1999) 649–651, https://doi.org/10.1038/23220.

[3] M.T. Mehran, M.Z. Khan, R.-H. Song, T.-H. Lim, M. Naqvi, R. Raza, B. Zhu, M. B. Hanif, A comprehensive review on durability improvement of solid oxide fuel cells for commercial stationary power generation systems, Appl. Energy 352 (2023) 121864, https://doi.org/10.1016/j.apenergy.2023.121864.

[4] Q. Xu, Z. Guo, L. Xia, Q. He, Z. Li, I. Temitope Bello, K. Zheng, M. Ni, A comprehensive review of solid oxide fuel cells operating on various promising alternative fuels, Energy Convers. Manag. 253 (2022) 115175, https://doi.org/10.1016/j.enconman.2021.115175.

[5] S. Vafaeenezhad, A.R. Hanifi, M.A. Laguna-Bercero, T.H. Etsell, P. Sarkar, Microstructure and long-term stability of Ni–YSZ anode supported fuel cells: a review, Materials Futures 1 (4) (2022) 042101, https://doi.org/10.1088/2752-5724/ac88e7.

[6] I. Sreedhar, B. Agarwal, P. Goyal, S.A. Singh, Recent advances in material and performance aspects of solid oxide fuel cells, J. Electroanal. Chem. 848 (2019) 113315, https://doi.org/10.1016/j.jelechem.2019.113315.

[7] C. Lenser, D. Udomsilp, N.H. Menzler, P. Holtappels, T. Fujisaki, L. Kwati, H. Matsumoto, A.G. Sabato, F. Smeacetto, A. Chrysanthou, S. Molin, 9 - solid oxide fuel and electrolysis cells, in: O. Guillon (Ed.), Advanced Ceramics for Energy Conversion and Storage, Elsevier, 2020, pp. 387–547, https://doi.org/10.1016/B978-0-08-102726-4.00009-0.

[8] L. Shu, J. Sunarso, S.S. Hashim, J. Mao, W. Zhou, F. Liang, Advanced perovskite anodes for solid oxide fuel cells: a review, Int. J. Hydrogen Energy 44 (59) (2019) 31275–31304, https://doi.org/10.1016/j.ijhydene.2019.09.220.

[9] S.-e. Hou, J.A. Alonso, J.B. Goodenough, Co-free, iron perovskites as cathode materials for intermediate-temperature solid oxide fuel cells, J. Power Sources 195 (1) (2010) 280–284, https://doi.org/10.1016/j.jpowsour.2009.07.017.

[10] J. Richter, P. Holtappels, T. Graule, T. Nakamura, L.J. Gauckler, Materials design for perovskite SOFC cathodes, Monatshefte für Chemie - Chemical Monthly 140 (9) (2009) 985–999, https://doi.org/10.1007/s00706-009-0153-3.

[11] K. Karuppiah, A.M. Ashok, Review of proton- and oxide-ion-conducting perovskite materials for SOFC applications, Nanomater. Energy 8 (1) (2019) 51–58, https://doi.org/10.1680/jnaen.18.00004.

[12] T. Wei, Q. Zhang, Y.-H. Huang, J.B. Goodenough, Cobalt-based double-perovskite symmetrical electrodes with low thermal expansion for solid oxide fuel cells, J. Mater. Chem. 22 (1) (2012) 225–231, https://doi.org/10.1039/C1JM14756K.

[13] Z. Li, M. Peng, Y. Zhao, J. Li, Y. Sun, Minimized thermal expansion mismatch of cobalt-based perovskite air electrodes for solid oxide cells, Nanoscale 13 (47) (2021) 20299–20308, https://doi.org/10.1039/D1NR06845H.

[14] R. Vinoth Kumar, A.P. Khandale, A review on recent progress and selection of cobalt-based cathode materials for low temperature-solid oxide fuel cells, Renew. Sustain. Energy Rev. 156 (2022) 111985, https://doi.org/10.1016/j.rser.2021.111985.

[15] N. Shah, X. Xu, J. Love, H. Wang, Z. Zhu, L. Ge, Mitigating thermal expansion effects in solid oxide fuel cell cathodes: a critical review, J. Power Sources 599 (2024) 234211, https://doi.org/10.1016/j.jpowsour.2024.234211.

[16] Q. Zhou, X. Zhang, Y. Wang, Y. Ma, H. Yang, A thermal-expansion offset to cobalt-based cathode materials for solid oxide fuel cells, Next Energy 5 (2024) 100168, https://doi.org/10.1016/j.nxener.2024.100168.

[17] Y. Wu, Z. Yan, J. Xu, Z. Zhong, X. Xu, Insight into mechanism of boosted oxygen reduction reaction in mixed-conducting composite cathode of solid oxide fuel cell via a novel open-source pore-scale model, Chem. Eng. J. 469 (2023) 143854, https://doi.org/10.1016/j.cej.2023.143854.

[18] G.C. Kostogloudis, P. Fertis, C. Ftikos, The perovskite oxide system Pr1−xSrxCo1−yMnyO3-δ: crystal structure and thermal expansion, J. Eur. Ceram. Soc. 18 (14) (1998) 2209–2215, https://doi.org/10.1016/S0955-2219(98)00169-1.

[19] B. Wei, Z. Lü, X. Huang, J. Miao, X. Sha, X. Xin, W. Su, Crystal structure, thermal expansion and electrical conductivity of perovskite oxides BaxSr1−xCo0.8Fe0.2O3−δ (0.3≤x≤0.7), J. Eur. Ceram. Soc. 26 (13) (2006) 2827–2832, https://doi.org/10.1016/j.jeurceramsoc.2005.06.047.

[20] A. Subardi, K.-Y. Liao, Y.-P. Fu, Oxygen permeation, thermal expansion behavior and electrochemical properties of LaBa0.5Sr0.5Co2O5+δ cathode for SOFCs, RSC Adv. 7 (24) (2017) 14487–14495, https://doi.org/10.1039/C7RA00125H.

[21] X. Zhang, S. Yu, M. Wang, S. Dong, J. Parbey, T. Li, M. Andersson, Thermal stress analysis at the interface of cathode and electrolyte in solid oxide fuel cells, Int. Commun. Heat Mass Tran. 118 (2020) 104831, https://doi.org/10.1016/j.icheatmasstransfer.2020.104831.

[22] Y. Wang, C. Wu, S. Zhao, Z. Guo, B. Zu, M. Han, Q. Du, M. Ni, K. Jiao, Assessing performance degradation induced by thermal cycling in solid oxide cells, Energy Convers. Manag. 270 (2022) 116239, https://doi.org/10.1016/j.enconman.2022.116239.

[23] A.M. Mehdi, A. Hussain, R.H. Song, T.-H. Lim, W.W. Kazmi, H.A. Ishfaq, M. Z. Khan, S. Qamar, M.W. Syed, M.T. Mehran, Improving the durability of cobaltite cathode of solid oxide fuel cells–a review, RSC advances 13 (36) (2023) 25029–25053.

[24] Y. Zhang, J. Li, H. Xie, Z. Liu, S. Shen, Y. Teng, D. Guan, S. Zhai, Y. Song, W. Zhou, B. Chen, M. Ni, Z. Shao, CO2-induced reconstruction for ORR-enhanced solid oxide fuel cell cathode, Chem. Eng. J. 462 (2023) 142216, https://doi.org/10.1016/j.cej.2023.142216.

[25] H. Su, Y.H. Hu, Progress in low-temperature solid oxide fuel cells with hydrocarbon fuels, Chem. Eng. J. 402 (2020) 126235, https://doi.org/10.1016/j.cej.2020.126235.

[26] R. Pelosato, G. Cordaro, D. Stucchi, C. Cristiani, G. Dotelli, Cobalt based layered perovskites as cathode material for intermediate temperature Solid Oxide Fuel Cells: a brief review, J. Power Sources 298 (2015) 46–67, https://doi.org/10.1016/j.jpowsour.2015.08.034.

[27] L. Zhang, M. Liu, J. Huang, Z. Song, Y. Fu, Y. Chang, C. Li, T. He, Improved thermal expansion and electrochemical performances of Ba0.6Sr0.4Co0.9Nb0.1O3−δ–Gd0.1Ce0.9O1.95 composite cathodes for IT-SOFCs, Int. J. Hydrogen Energy 39 (15) (2014) 7972–7979, https://doi.org/10.1016/j.ijhydene.2014.03.055.

[28] A.K. Yadav, S. Sinha, A. Kumar, Advancements in composite cathodes for intermediate-temperature solid oxide fuel cells: a comprehensive review, Int. J. Hydrogen Energy 59 (2024) 1080–1093, https://doi.org/10.1016/j.ijhydene.2024.02.124.

[29] Y. Zhang, B. Chen, D. Guan, M. Xu, R. Ran, M. Ni, W. Zhou, R. O'Hayre, Z. Shao, Thermal-expansion offset for high-performance fuel cell cathodes, Nature 591 (7849) (2021) 246–251, https://doi.org/10.1038/s41586-021-03264-1.

[30] N. Shah, T. Zhu, D. Feng, X. Xu, F. Liang, H. Wang, Z. Zhu, L. Ge, Fine-tuning thermal expansion characteristics of solid oxide fuel cell cathode via composite cathode fabrication, J. Power Sources 616 (2024) 235143, https://doi.org/10.1016/j.jpowsour.2024.235143.

[31] K. Liu, F. Lu, X. Jia, H. He, J. Su, B. Cai, A high performance thermal expansion offset composite cathode for IT-SOFCs, J. Mater. Chem. A 10 (45) (2022) 24410–24421, https://doi.org/10.1039/D2TA04899J.

[32] L. Hu, D. Zhou, X. Zhu, N. Wang, J. Bai, H. Gong, Y. Zhang, Y. Chen, W. Yan, Q. Zhu, A high-performance composite cathode based on thermal expansion complementation for SOFC, Fuel 362 (2024) 130864, https://doi.org/10.1016/j.fuel.2024.130864.

[33] F. Lu, Y. Shi, L. Shi, M. Li, R. Cui, J. Wang, H. He, J. Su, J. Wang, B. Cai, Improved SOFC performance by enhancing cathode/electrolyte bonding and grain refinement of cathode with thermal expansion offset, Ceram. Int. (2024), https://doi.org/10.1016/j.ceramint.2024.08.474.

[34] M. Li, F. Lu, R. Cui, L. Shi, J. Wang, H. He, J. Su, B. Cai, High performance thermal expansion offset LSCF-SZM cathodes of IT-SOFCs, Solid State Ionics 414 (2024) 116639, https://doi.org/10.1016/j.ssi.2024.116639.

[35] S.M. Hassan, S.A. Hasnain, Measuring porosity of anodes in solid oxide fuel cell (SOFC) through water archimedeans porosimetry, J. Power Energy Eng. 3 (2015) 46–53.

[36] Q. Zeng, X. Zhang, W. Wang, D. Zhang, Y. Jiang, X. Zhou, B. Lin, A Zn-doped Ba0.5Sr0.5Co0.8Fe0.2O3-δ perovskite cathode with enhanced ORR catalytic activity for SOFCs, Catalysts (2020).

[37] P. Wang, Z. Xu, X. Liu, H. Wang, B. Qin, J. Lin, J. Cao, J. Qi, J. Feng, Regulating the interfacial reaction of Sc2W3O12/AgCuTi composite filler by introducing a carbon barrier layer, Carbon 191 (2022) 290–300, https://doi.org/10.1016/j.carbon.2022.01.065.

[38] W. Miller, C.W. Smith, D.S. Mackenzie, K.E. Evans, Negative thermal expansion: a review, J. Mater. Sci. 44 (20) (2009) 5441–5451, https://doi.org/10.1007/s10853-009-3692-4.

[39] M.A. Yatoo, S.S. Kawale, S.J. Skinner, Chapter 9 - perovskite and layered oxide materials for intermediate temperature solid oxide fuel cells, in: G. Kaur (Ed.), Intermediate Temperature Solid Oxide Fuel Cells, Elsevier, 2020, pp. 315–346, https://doi.org/10.1016/B978-0-12-817445-6.00010-7.

[40] A. Ndubuisi, S. Abouali, K. Singh, V. Thangadurai, Recent advances, practical challenges, and perspectives of intermediate temperature solid oxide fuel cell cathodes, J. Mater. Chem. A 10 (5) (2022) 2196–2227, https://doi.org/10.1039/D1TA08475E.

[41] M. Choi, W. Lee, Tuning the oxygen vacancy concentration in a heterostructured electrode for high chemical and electrochemical stabilities, Chem. Eng. J. 431 (2022) 134345, https://doi.org/10.1016/j.cej.2021.134345.

[42] W. Zhou, R. Ran, Z. Shao, W. Jin, N. Xu, Evaluation of A-site cation-deficient (Ba0.5Sr0.5)1−xCo0.8Fe0.2O3−δ (x>0) perovskite as a solid-oxide fuel cell cathode, J. Power Sources 182 (1) (2008) 24–31, https://doi.org/10.1016/j.jpowsour.2008.04.012.

[43] K. Zou, M. Jiang, Z. Zhao, S. Xie, T. Ning, L. Tan, H. Li, Y. Zhou, W. Wang, X. Wu, L. Li, Mechanistic insights into suppressing microcracks by regulating grain size of precursor for high-performance Ni-rich cathodes, Chem. Eng. J. 476 (2023) 146793, https://doi.org/10.1016/j.cej.2023.146793.

[44] T. Yang, Y. Fan, J. Liu, H. Finklea, S. Lee, B. Guan, H.W. Abernathy, T.L. Kalapos, G.A. Hackett, Multiphysics modeling of SOFC performance degradation caused by interface delamination and active layer cracking, Int. J. Hydrogen Energy 47 (97) (2022) 41124–41137, https://doi.org/10.1016/j.ijhydene.2022.09.194.

[45] F. Xue, Y. Lei, T.-L. Cheng, W.K. Epting, G. Hackett, H. Abernathy, Y.-H. Wen, Phase-field modeling of crack growth and mitigation in solid oxide cells, Int. J. Hydrogen Energy 48 (26) (2023) 9845–9860, https://doi.org/10.1016/j.ijhydene.2022.12.042.

[46] X. Wang, Z. Chen, A. Atkinson, Crack formation in ceramic films used in solid oxide fuel cells, J. Eur. Ceram. Soc. 33 (13) (2013) 2539–2547, https://doi.org/10.1016/j.jeurceramsoc.2013.04.032.

[47] S. Yang, Y. Lu, K. Wang, X. Zhao, F. Wang, Defect transport and thermal mismatch induced fracture in planar solid oxide fuel cell, Int. J. Electrochem. Sci. 19 (8) (2024) 100678, https://doi.org/10.1016/j.ijoes.2024.100678.

[48] Q. Shao, R. Fernández-González, J.C. Ruiz-Morales, L. Bouhala, D. Fiorelli, A. Younes, P. Núñez, S. Belouettar, A. Makradi, An advanced numerical model for energy conversion and crack growth predictions in Solid Oxide Fuel Cell units, Int. J. Hydrogen Energy 40 (46) (2015) 16509–16520, https://doi.org/10.1016/j.ijhydene.2015.10.016.

[49] H. Yakabe, Y. Baba, T. Sakurai, Y. Yoshitaka, Evaluation of the residual stress for anode-supported SOFCs, J. Power Sources 135 (1) (2004) 9–16, https://doi.org/10.1016/j.jpowsour.2003.11.049.

[50] Q. Shao, R. Fernández-González, A. Mikdam, L. Bouhala, A. Younes, P. Núñez, S. Belouettar, A. Makradi, Influence of heat transfer and fluid flow on crack growth in multilayered porous/dense materials using XFEM: application to Solid Oxide Fuel Cell like material design, Int. J. Solid Struct. 51 (21) (2014) 3557–3569, https://doi.org/10.1016/j.ijsolstr.2014.06.011.

[51] A. Atkinson, Chemically-induced stresses in gadolinium-doped ceria solid oxide fuel cell electrolytes, Solid State Ionics 95 (3) (1997) 249–258, https://doi.org/10.1016/S0167-2738(96)00588-7.

[52] J. Malzbender, E. Wessel, R.W. Steinbrech, Reduction and re-oxidation of anodes for solid oxide fuel cells, Solid State Ionics 176 (29) (2005) 2201–2203, https://doi.org/10.1016/j.ssi.2005.06.014.

[53] J. Malzbender, W. Fischer, R.W. Steinbrech, Studies of residual stresses in planar solid oxide fuel cells, J. Power Sources 182 (2) (2008) 594–598, https://doi.org/10.1016/j.jpowsour.2008.04.035.

[54] M. Liang, Y. Zhu, Y. Song, D. Guan, Z. Luo, G. Yang, S.P. Jiang, W. Zhou, R. Ran, Z. Shao, A new durable surface nanoparticles-modified perovskite cathode for protonic ceramic fuel cells from selective cation exsolution under oxidizing atmosphere, Adv. Mater. 34 (10) (2022) 2106379, https://doi.org/10.1002/adma.202106379.

[55] J.H. Kim, J.K. Kim, H.G. Seo, D.-K. Lim, S.J. Jeong, J. Seo, J. Kim, W. Jung, Ex-solved Ag nanocatalysts on a Sr-free parent scaffold authorize a highly efficient route of oxygen reduction, Adv. Funct. Mater. 30 (27) (2020) 2001326, https://doi.org/10.1002/adfm.202001326.

[56] Q. Lv, Y. Liu, F. Han, H. Xia, Q. Zhou, Z. Zhang, B. Xu, H. Shi, Performance analysis of cathode materials SSC-xYWO (x = 0–30 wt. %) based on thermal expansion complementarity for SOFCs, Electrochim. Acta 514 (2025) 145645, https://doi.org/10.1016/j.electacta.2025.145645.

[57] Y. Gao, M. Fu, S. Zhao, Z. Hou, K. Liu, X. Deng, Z. Tao, Self-assembled composite cathodes with TEC gradient for proton-conducting solid oxide fuel cells, Adv. Funct. Mater. 35 (10) (2025) 2416625, https://doi.org/10.1002/adfm.202416625.

[58] X. Xu, J. Zhao, M. Li, L. Zhuang, J. Zhang, S. Aruliah, F. Liang, H. Wang, Z. Zhu, Sc and Ta-doped SrCoO3-δ perovskite as a high-performance cathode for solid oxide fuel cells, Compos. B Eng. 178 (2019) 107491, https://doi.org/10.1016/j.compositesb.2019.107491.

[59] X. Mao, Z. Li, M. Li, X. Xu, C. Yan, Z. Zhu, A. Du, Computational design and experimental validation of the optimal bimetal-doped SrCoO3−δ perovskite as solid oxide fuel cell cathode, J. Am. Chem. Soc. 143 (25) (2021) 9507–9514, https://doi.org/10.1021/jacs.1c03441.

[60] Z. Li, X. Mao, D. Feng, M. Li, X. Xu, Y. Luo, L. Zhuang, R. Lin, T. Zhu, F. Liang, Z. Huang, D. Liu, Z. Yan, A. Du, Z. Shao, Z. Zhu, Prediction of perovskite oxygen vacancies for oxygen electrocatalysis at different temperatures, Nat. Commun. 15 (1) (2024) 9318, https://doi.org/10.1038/s41467-024-53578-7.

[61] M. Li, M. Zhao, F. Li, W. Zhou, V.K. Peterson, X. Xu, Z. Shao, I. Gentle, Z. Zhu, A niobium and tantalum co-doped perovskite cathode for solid oxide fuel cells operating below 500 °C, Nat. Commun. 8 (1) (2017) 13990, https://doi.org/10.1038/ncomms13990.